

# Computations of Flapping Flow Propulsion for UUV Design

Ravi Ramamurti<sup>\*</sup> and Jason Geder  
Laboratory for Computational Physics and Fluid Dynamics,  
*Naval Research Laboratory, Washington, DC 20375-5344, USA*

John Palmisano and Banahalli Ratna  
Center for Bio-Molecular Science and Engineering  
*Naval Research Laboratory, Washington, DC 20375-5344, USA*

William C. Sandberg<sup>†</sup>  
*Science Applications International Corporation, McLean, VA 22102, USA*

## Abstract

Three-dimensional unsteady computations of the flow past a flapping and deforming fin are performed. The computed unsteady lift and thrust force time histories are validated with experimental data and are in good agreement. Several fin parametric studies are performed for a notional Unmanned Underwater Vehicle (UUV). The parametric studies investigated the force production of the fin as a function of varying the flexibility, the bulk amplitude of fin rotation, the vehicle speed and the fin stroke bias angle. The results of these simulations are used to evaluate the hydrodynamic performance of the vehicle and to support controller development. Computations are also performed to map out the hydrodynamic characteristics of a new test vehicle, designed and built at NRL to demonstrate the hovering and low-speed maneuvering performance of a set of actively controlled curvature fins.

## I. Introduction

Unmanned underwater vehicles (UUVs) have demonstrated their capabilities in applications including inspection, surveillance, exploration and object detection. These capabilities are of

---

<sup>\*</sup> Aerospace Engineer, Associate Fellow, AIAA

<sup>†</sup> Senior Member, AIAA

considerable value, particularly in environments that are dangerous or impossible for a human to navigate. Current technology has allowed UUVs to excel at tasks including deep-sea diving, high-speed motion and long distance traversal. The low-speed, high maneuverability operations required of many near-shore and littoral zone missions present different mobility challenges that may require different solutions.

Flapping fins are an attractive alternative to thrusters for overcoming the difficulties associated with low-speed maneuverability in the presence of ocean currents and near-shore obstacles. Aquatic animals certainly achieve high levels of controllability at near-zero forward speed. Blake<sup>1</sup> determined that in low-speed operations labriform motion (using pectoral fin oscillation) is more efficient for maneuvering than carangiform motion (using body and caudal fin undulation). This result suggests that a flapping pectoral fin can be mounted on a rigid UUV hull without sacrificing low-speed maneuverability. Many investigators have studied fin propulsion both theoretically and experimentally. There have been several comprehensive surveys published summarizing the history in this field, such as those by Platzer and Jones<sup>2</sup>, Rozhdestvensky and Ryzhov<sup>3</sup>, and Shyy et al<sup>4</sup>. Many experimental investigations have also been carried out to study the performance of oscillating surfaces as propulsors installed in unmanned underwater vehicles. Kato et al.<sup>5</sup> and Ando et al.<sup>6</sup> have developed and incorporated both lift-based and drag-based deformable pectoral fins into unmanned underwater vehicles. Tangorra et al.<sup>7</sup> have developed a flapping fin based on the bluegill sunfish for use as a propulsor. They have used CFD simulations and proper orthogonal decomposition analysis to identify the first few modes of measured fin deformation that produce the majority of the force. This has enabled them to avoid trying to replicate the entire measured fin deformation time-history. None of these previous flapping fin propulsor investigations have, however, provided the capability to initially

predict the precise temporal surface curvature variation needed to create a specified mission force time-history. One of the distinguishing features of our research is that we have computed the deforming fin force time-histories first, as a function of fin surface curvature variation, to achieve a desired vehicle hovering and maneuvering performance. Our deforming fin was subsequently developed with the active deformation needed to produce that surface curvature time-variation.

Walker and Westneat<sup>8</sup> have studied the fin kinematics of a class of lift-based labriform fish, the bird wrasse (*gomphosus varius*), whose force production is a good match with our performance objectives. Ramamurti et al.<sup>9</sup> computationally studied the force production of the bird wrasse and achieved good agreement with Walker and Westneat<sup>8</sup>. The computational method used to study the force production of the bird wrasse has been applied to the design and development of an actively controlled-curvature biomimetic pectoral fin by Palmisano et al<sup>10</sup>. The resulting actuated fin design has been built and incorporated into a prototype test vehicle for demonstrating its dynamic performance in propulsion and low-speed maneuvering.

We have chosen a two-fin test vehicle design in order to demonstrate deforming fin force production with vertical plane and yaw control in an underwater environment, using a simple vehicle configuration. The primary objectives of the current study are to select the shape of the fin that allows flexibility while keeping mechanical system less complex. In-water laboratory experiments of the stand-alone fin to obtain deformation time-history and the associated fin force production time-history have already been carried out and those results are described below. The computational results using an unstructured grid based Navier-Stokes solver, *feFlo*, are validated against this experimental data. Three-dimensional unsteady computations of a notional Unmanned Underwater Vehicle with flapping fins are also carried out. Several parametric

studies varying the amplitude and frequency of oscillation of the fin, the flexibility of the fin and the stroke bias angle are performed. The objective of these computations is to create force time histories for a range of operating conditions of the vehicle. The results of the computations are used to map the forces to kinematics. This mapping will be used for controller development and to evaluate the vehicle performance.

## II. The Incompressible Flow Solver

The governing equations employed are the incompressible Navier-Stokes equations in Arbitrary Lagrangian-Eulerian (ALE) formulation which are written as

$$\frac{d\mathbf{v}}{dt} + \mathbf{v}_a \cdot \nabla \mathbf{v} + \nabla p = \nu \nabla^2 \mathbf{v}, \quad (1)$$

$$\nabla \cdot \mathbf{v} = 0, \quad (2)$$

where  $p$  denotes the pressure,  $\nu$  is the kinematic viscosity,  $\mathbf{v}_a = \mathbf{v} - \mathbf{w}$  the advective velocity vector, where  $\mathbf{v}$  is the flow velocity and  $\mathbf{w}$  is the mesh velocity and the material derivative is with respect to the mesh velocity  $\mathbf{w}$ . Both the pressure  $p$  and the viscous stress tensor have been normalized by the (constant) density  $\rho$  and are discretized in time using an implicit time stepping procedure. Thus the equations are Eulerian for zero mesh velocity and Lagrangian if the mesh velocity is the same as the flow velocity. The present time-accurate flow solver is discretized in space using a Galerkin procedure with linear tetrahedral elements. The details of the flow solver have already been discussed extensively elsewhere (Ramamurti et al.<sup>11, 12</sup>) in connection with successfully validated solutions for numerous 2-D and 3-D, laminar and turbulent, steady and unsteady flow problems.

### III. Results and Discussion

Ramamurti and Sandberg<sup>13</sup> have computed the unsteady flow past a UUV with flapping fins. They have studied the effect of varying the amplitude and frequency of oscillation of the fin and the angle of attack at the root of the fin. They found that the near optimum parameters for enabling the vehicle to hover in a 3kt current, to be a fin root angle of attack of  $20^\circ$  ( $\alpha_r$ ), with the fin flapping at a frequency of 2Hz and a fin stroke amplitude of  $114^\circ$ . The angle of attack  $\alpha_r$  in that study was the angle the root of the fin chord with respect to the inflow direction, shown in Fig. 1. In the present effort, the *feFlo* incompressible flow solver is used to compute the unsteady three dimensional flow past an isolated flapping fin at hovering conditions and is validated by comparisons with the in-water experimental data measured at NRL. Computations are performed to investigate the effects on force production by varying parameters such as the vehicle speed, flapping frequency, the flexibility of the fin and the starting location of the downstroke of the fin. The results of these simulations are coupled with the test vehicle hydrodynamic characteristics and incorporated into the development of the vehicle controller so as to enable a stable and maneuverable UUV.

#### A. Fin Design and Test Setup

Ramamurti and Sandberg<sup>14</sup> have studied the effect of variable rigidity of the Bird-wrasse fin on the fluid dynamics of force production. Based on this study, we have reduced the number of ribs of the mechanical fin from 14 spines in the fish to 5 equally spaced ribs, in order to reduce the complexity of the mechanical system while maintaining enough flexibility of the fin surface to achieve the curvature computed to be necessary. An actively deforming mechanical fin has been designed using compliant ribs and built by Palmisano et al<sup>10</sup>. This experimental design and setup is shown in Fig. 2. The fin rib is a compliant structure, designed to bend to a specific base

to tip deflection angle when subjected to translational forces at the base of the rib. The topology of the compliant ribs was designed using a structural-optimization based on synthesis approach by Trease et al.<sup>15</sup>. The fin is comprised of five such ribs each actuated by a single servo motor. The phasing of the actuators is specified in conjunction with the bulk rotation of the entire fin, to obtain the desired instantaneous shape throughout the stroke. In addition to the actuation of each individual rib, the bulk rotation of the fin throughout the flapping cycle is controlled by a servo motor. The entire set of five ribs is encased in a liquid silicone rubber skin that is designed to elastically deform. A small water tank (76cm × 30cm × 46cm) is used to test the actuation of the fin. In this initial setup, a torque cell and a load cell, coaxial with the bulk rotation axis, are used to measure the thrust, lift and the moment about the axis. In order to protect the expensive load and torque sensors, the fin rotation axis in the experiment is located at 1.3cm above the water surface. This led to a drawback in the measurement setup that the fin surface is not fully submerged underwater.

The force measurement device is modified using a gantry described by Palmisano et al.<sup>16</sup>, shown in Fig. 3, so that the fin is fully submerged underwater. Also, a pair of torque sensors placed orthogonal to each other replaces the coaxial load cell and the torque cells. One of the torque cell measures the fin thrust, while the second one measures the lift force and the moment. In order to derive the forces from the torque cell measurements, the span wise location of the center of pressure on the fin is needed in addition to the offset of the axis of fin rotation from the sensor axis and the bulk rotation angle. The location of the center of pressure is obtained from the computations performed with the rigid fin and it remains nearly constant at 0.06m from the root of the fin.

The kinematics of the flapping fin is obtained using the two high-speed camera system shown in Fig. 2a and described in by J. Geder et al<sup>17</sup>. The two cameras are positioned nearly orthogonal to each other, to maximize the accuracy of the position measurements since this arrangement provides the most unique field of view for each of the cameras. The set of two 2-D camera pixel coordinates is then converted to a single 3-D world coordinates. To calibrate this camera system, we must collect image of points with known 3-D location covering the space that the fin will operate. For this purpose, a structure of LEGO bricks is devised and suspended in the field of interest. Sufficient points to cover the field of interest are marked on this structure and 2-D pixel coordinates from both cameras and the actual 3-D coordinate of the points are recorded. The tips of the 5 ribs of the fin described in the previous section are marked. Their location in space and time throughout the stroke will describe the kinematics of the fin tip.

In the computations, the deforming shape of the fin is constructed using a spline line passing through the tips of the ribs and the root of the rib, shown in Fig. 1. Therefore, the deforming shape of the fin is controlled by the prescribed motion of the tips of the ribs and does not include the fluid structure interaction on the surface of the fin. More precise kinematics of the deforming fin could be obtained if one were to use an array of markers distributed on both the surfaces of the fin, but this will involve additional camera systems as all the markers will not be visible in a 2-camera system at all instants during the flapping cycle due to the opaque skin and also the variable thickness of the fin.

In the initial setup, in order to obtain the bulk rotation of the root of the fin, the angle by which the fin tip of the third rib is rotated about the axis is used since this rib is not actuated. But high-speed videos of this initial setup showed that this rib does bend. Hence, in the new set up,

an additional rigid marker rod was added downstream of the trailing edge to correctly measure the bulk rotation angle.

## B. Baseline Kinematics

The deforming motion of the fin shown in Fig. 1 is obtained by prescribing the motion of the 5 control points or the tips of the rib (1-5). The kinematics of the ribs is decomposed into two motions. The first is a rotation of all the ribs about the fin axis of rotation termed as the bulk rotation, Fig. 4a, and the second is a supplemental rib rotation which is crucial for obtaining the deforming shape of the fin, Fig. 4b. The combined motion can be written as

$$\phi_i(t) = k_b \phi_{bulk}(t) + k_f \phi_{rel(i)}(t) + \phi_0, \quad i = 1,5 \quad (3)$$

where  $k_b$  and  $k_f$  are factors that can be varied to achieve various bulk amplitudes and relative flexibility, respectively, and  $\phi_0$  is the starting position of the downstroke of the fin. This baseline kinematics that mimics the Bird-wrasse was used by Ramamurti and Sandberg<sup>10</sup> and in this paper to study the effect of bulk amplitude, deformation of the fin and the flapping frequency.

In this study, prescribing the 5 fin tip locations controls the deforming shape of the fin. The different relative rotations of each of the rib give rise to the deforming shape of the fin throughout the stroke. Figure 5a shows the relative rotation of the leading and trailing edge ribs for three different deformation factors,  $k_f$ . The maximum difference between the relative rotations between these two ribs increased from a value of  $8.75^\circ$  for  $k_f = 0.5$  to  $26.25^\circ$  for  $k_f = 1.5$ . The variation of the wetted surface area of the fin throughout the stroke is shown in Fig. 5b, and it increases from a minimum of  $9.5 \text{ in}^2$  for the rigid fin ( $k_f = 0.0$ ) to a maximum of  $10.9 \text{ in}^2$  fully flexible fin ( $k_f = 1.5$ ).



### **C. Validation of CFD Results for a Rigid Fin**

The force time-history experimental data was obtained for a rigid fin by turning off the actuation of the individual ribs and retaining only the bulk rotation. The measured kinematics of the rigid flapping fin is shown in Fig. 6. The amplitude of the fin oscillation is  $110.7^\circ$ . The computed force time history is shown in Fig. 7. The mean thrust obtained from the computation is 0.078N and the mean lift during the cycle is -0.13 N. In order to obtain the lift and thrust forces from the experimental data, the mean moment arm is required. This was obtained by computing the center of pressure from the computations, shown in Fig. 7c. For the case of this rigid fin, the center of pressure remains nearly constant at 0.06m. This value was used in deriving the forces from the experimental data. Fig. 7b shows a good comparison of the computed lift with that of the experiments. The force transducer used in this set up was not able to capture the variation during the cycle as the sensitivity of this transducer was nearly 0.13N and the maximum variation in the thrust throughout the stroke is less than 0.2N. Also, in this initial setup, in order to protect the expensive load and torque sensors from water damage, the fin rotation axis was located above the water surface. This resulted in indeterminable surface interactions, such as waves and air ingestion that covered part of the root section of the fin. Hence, the experimental set up was modified using a gantry. This allowed the entire fin to be submerged in a larger tank while transferring the moments to the two crosswise mounted torque sensors.

### **D. Validation for a Deforming Fin**

With the improved experimental setup, a new set of kinematics was programmed into the rib actuator servos, shown in Fig. 8. This set yielded a bulk rotation amplitude of  $111.6^\circ$ , with the leading edge rib having an amplitude of  $103^\circ$  and the trailing edge rib with an amplitude of

126.5°. Although the amplitude of the ribs are opposite of that of the Bird-wrasse, where the amplitude of the leading edge is larger compared to the trailing edge, computations were performed with this set of kinematics. Also, for the fin flapping at 1.0715 Hz, the period of upstroke is 0.433 s and period of downstroke is 0.5 s. In contrast, the Bird wrasse fin has a 1:2 ratio between the periods of up and down strokes.

Figure 9 shows the comparison of the thrust and lift production between the CFD results and the experimental data. The comparison of the computed thrust time history is very good with the experimental results and the lift results compare reasonably well during the downstroke and do not capture the peaks during the upstroke. The mean thrust and lift produced in this case from the CFD results are 0.058 N and 0.005 N, respectively. The corresponding mean thrust and lift forces from the experimental data are 0.059 N and -0.052 N, respectively. Figure 10 shows the variation of the moment about the axis of rotation and the center of pressure on the fin from the computed results. Figure 10b shows that the moment arm varies between 0.045m and 0.065m during the stroke with the mean moment arm remaining nearly at 0.058m.

Figure 11 shows the velocity vector at a plane cut 0.0635m from the root of the fin. At  $t = 1.304$  s, just before the stroke reversal, we see the leading edge vortex shed below the fin, Fig. 11a, and after stroke reversal to downstroke, at  $t = 1.4578$  s, the leading and trailing edge vortices are seen above the fin, Fig. 11b. Close to this instant the thrust produced reaches a maximum. During the middle of the downstroke,  $t = 1.706$  s, an attached leading edge vortex is seen from Fig. 11c, and at  $t = 1.7037$  s, Fig. 11d, this vortex is elongated and detaches from the leading edge before  $t = 1.8367$  s, Fig. 11e, where the thrust produced is a minimum during the downstroke. Just after stroke reversal into the upstroke,  $t = 1.8999$  s, Fig. 11f, we can see both leading and trailing edge vortices formed, and the trailing edge vortex being shed into the wake,

Fig. 11g and the leading edge vortex elongates as the upstroke proceeds. These results show the qualitative wake features during the flapping cycle. Extreme caution has to be applied if one has to use the wake measurements in order to arrive at the forces produced by the flapping fin. Bohl and Koochesfahani<sup>18</sup> have recently shown that using only the mean velocity in the wake to obtain the forces leads to higher thrust coefficient compared to using the additional fluctuating components of the wake velocity. They have shown that using the complete wake velocity the experimental force coefficients matched well with the CFD results of Ramamurti and Sandberg<sup>19</sup> for a 2-D oscillating NACA 0012 airfoil. Figure 12 shows the instantaneous particle traces released from a rake just in front of the leading edge, Figs. 12a-d, just before the stroke reversal into the downstroke,  $t = 1.3065$ s, during the mid downstroke,  $t = 1.6713$  s, just after stroke reversal into the upstroke,  $t = 1.9428$ s and during the middle of the upstroke,  $t = 2.0575$ s. These traces show the presence of the leading edge vortex that detaches from the surface of the fin in the middle of the span. Also, the span wise flow in the core of the vortex is seen form to extend from the middle of the span to the wing tip, Figs. 12c and d. Similar span wise flow is also observed in the particle traces released from near the trailing edge just before the stroke reversal,  $t = 1.3065$ s. The trailing edge vortex that was shed after stroke reversal into the upstroke,  $t = 1.428$  s, is also seen in Fig. 12f.

A grid refinement study was conducted to assess the sensitivity of the computed results to spatial resolution. The mesh spacing near the fin was halved and that the total number of grid points in the computational domain increased from 161 K points to 384 K points. Figure 13 shows the effect of grid refinement on the force production. It is clear that the mesh with 161 K points is sufficient. The effect of viscosity on the force production was investigated by carrying out the simulation was performed with a finer mesh of 384 K points and a Smagorinsky<sup>20</sup>

turbulence model. The Reynold's number,  $Re$ , for the viscous computation was 13,400 based on mean tip speed,  $V_{tip} = 0.4175$  m/s and the mean chord of the fin,  $\bar{c} = 0.03205$  m. The results show that the effect of viscosity is minimal, Fig. 14. This confirms our earlier findings on flapping insect wings, Ramamurti and Sandberg<sup>21</sup> and fish fins, Ramamurti et al.<sup>9</sup>, that the force production is inertially dominated.

In order to understand the differences in the lift production during the upstroke, another set of kinematics that mimics the Bird-wrasse was programmed into the servos for the ribs. The bulk rotation angle was measured using the additional marker rod instead of using rib 3. The experimental kinematics is shown in Fig. 15a. It was smoothed based on the acceleration of the tips of the ribs, resulting in the kinematics shown in Fig. 15b. The amplitude of the bulk rotation of the fin  $130^\circ$ , the amplitude of the leading edge rib is  $147^\circ$  and that of the trailing edge is  $131.3^\circ$ . Although the upstroke is slower than the desired Bird-wrasse kinematics, the phasing of the individual ribs and the amplitude are closer to it.

With these set of kinematics, the computed results were compared to the experimentally obtained thrust and lift, shown in Fig. 16. The computed results using the raw and the smoothed kinematics envelop the force time history obtained experimentally and the agreement is good in terms of thrust. The experimental lift curves still exhibit peaks outside the CFD envelope. The reason for this could be the use of a constant moment arm in the case of deforming fin for the data reduction. Another reason for the differences is that in the experiments the surface of the fin deforms due the fluid structure interaction which is not modeled in the computations. In the remainder of the study, the computations are performed based on an idealized baseline kinematics obtained from the Bird-wrasse kinematics and varying other pertinent controllable parameters.

## E. Parametric Studies

The controllable fin parameters that were varied in this study are the bulk amplitude, relative deformability of the fin, flapping fin frequency, starting position of the downstroke and the vehicle speed. Simulations were performed across all these parameters and the results are summarized below.

First, we summarize the effect of vehicle speed on the thrust and lift generation of a fin flapping at 2 Hz. For this simulation,  $k_b$  and  $k_f$  were set to 1.5 and  $\phi_0 = -85^\circ$ . Figure 17 shows the variation of thrust and lift production for vehicle speeds ranging from hovering to a vehicle moving at 3kts. As the vehicle speed is increased, the mean thrust produced decreases. The flapping fin is able to provide positive thrust up to 2kts. The mean lift also decreases with increase in vehicle speed, Fig. 17b, and the lift excursion also increases, especially during the upstroke. This suggests that modification of the fin kinematics is necessary if we wish to operate above 2 kts. Since we are primarily interested in the 0-2 kt range we have not pursued this yet. Next, the flexibility of the fin was varied from a rigid fin ( $k_f = 0.0$ ) to a fully flexible fin ( $k_f = 1.5$ ). For this test, the vehicle speed of 1kt and a flapping frequency of 1 Hz were maintained constant. As the fin is made more flexible, the mean thrust produced increases nearly four fold, Fig. 18a, from a rigid fin, 0.065N, to a fully flexible fin, 0.238 N. The rigid fin produces drag during the downstroke while the flexible fins produce positive thrust. This positive effect is offset by the loss of lift in the flexible fins, shown in Fig. 18b. The surface pressure distribution on the top and bottom surfaces of the fin at an instant when the thrust reaches a maximum during the downstroke,  $t = 1.09$  s, for the flexible fin is shown in Fig. 19a and b. The rigid fin at the same instant shows a much lower pressure on the top surface, Fig. 19d and a higher pressure on the bottom surface, Fig. 19e, compared to that of the flexible fin. Figures 19c and f show the

resultant force vector and the orientation of the fin at this instant. For clarity, the transverse component of the force vector is zeroed out and the vector is not drawn to scale. It is clear that the resultant force for the flexible fin is in the negative  $x$ -direction, but for the rigid fin is along the  $x$ -axis yielding a drag force.

The effect of the amplitude of fin rotation was studied by choosing  $k_b = \{1.25, 1.5, 1.75\}$ . This resulted in a bulk amplitude of  $89.6^\circ$ ,  $107.6^\circ$  and  $125.5^\circ$ , respectively. For this study, a fully flexible fin,  $k_f = 1.5$ , was used with the vehicle speed of 1 kt and the flapping frequency of 2 Hz maintained constant. As expected, as the amplitude is increased the mean lift decreased and thrust forces increased. The mean thrust increased from 0.1615 N to 0.2377 N and achieved a maximum of 0.3132 N; the mean lift increased from -0.2087 N to -0.2345 N and achieved a maximum of -0.2731 N. When the forces were normalized using

$$C_F = \frac{F}{\frac{1}{2}\rho V_{tip}^2 A_{fin}}, \quad (4a,b)$$

$$V_{tip} = 2\phi_{bulk} R f$$

where  $\rho$  is the density of water,  $R$  is the length of the leading edge rib,  $f$  is the flapping frequency,  $V_{tip}$  is the mean velocity of the fin tip and  $A_{fin}$  is the average area of the fin during the stroke, the force time history collapses into one curve as shown in Fig. 20a and b. Similar results are obtained by increasing the frequency of flapping from 1 Hz to 2 Hz, as shown in Fig. 21. Although both the lift and thrust coefficients collapse reasonably well during the upstroke of the flapping cycle, they are different during the downstroke of the cycle. This is due to the fact that the pressure distribution on the bottom surface of the fin although remains qualitatively similar, Figs. 22a and c, the pressure distribution for the 2Hz case on the top surface of the fin exhibits lower pressure and unsteadiness, Fig. 22b. For a hovering vehicle,  $V = 0$  kts, the coefficients of

thrust and lift for the two frequencies studied collapse into a single curve as shown in Fig. 23 a and b. The purpose of computing the forces coefficients in this research effort is to guide the controller design to properly interpolate between the various bulk amplitudes and the frequencies of interest and not to arrive at a universal force coefficient that encompasses all the parameters. In order to arrive at the proper scaling of the forces, the forward speed of the vehicle, i.e., an advance ratio with respect to the fin tip speed, the angle of attack of the root of the fin with the incoming flow, in addition to the amplitude and frequency, has to be taken into account, which is beyond the scope of this paper.

Identification of sets of kinematics that will yield positive lift forces is an important aspect of the design of a controller for steady level flight. One way to achieve the lift is to vary the flexibility of the fin as shown here, but this is accompanied by the loss of thrust. Another method to obtain mean positive lift is to change the starting location of the downstroke. In this study, three starting locations were considered. Simulations were performed by varying  $\phi_0 = \{-85^\circ, -65^\circ, -45^\circ\}$  for  $k_b = \{1.25, 1.5, 1.75\}$  and  $k_f = \{0., 0.5, 1.0, 1.5\}$ . Figure 23 shows the mean thrust and lift generated as a function of the bulk amplitude, fin flexibility and the starting location of the downstroke. For clarity of visualization, the surfaces corresponding to  $\phi_0 = -85^\circ$  and  $-45^\circ$  are shifted by  $\pm 0.1$  N. As the fin flexibility is decreased, the mean lift increases almost linearly while the other two parameters are fixed. A similar effect is achieved by changing the starting location of the downstroke. The range of mean thrust and lift forces obtained by varying fin flexibility and downstroke starting location suggests that these are viable control parameters for vertical stability of the UUV.

## **F. Hydrodynamic Characteristics of NRL-UUV**

A new test vehicle shown in Fig. 25a, has been designed, Palmisano et al.<sup>16</sup>, which carries a set of two actively controlled curvature fins in order to demonstrate thrust production and vertical plane controllability in an underwater test environment. The performance of a newly developed UUV under various swimming speeds,  $V = 1\text{kt}$  and  $2\text{kts}$ , and pitch angle of attack,  $\alpha = 0^\circ$  to  $30^\circ$  and side slip angles,  $\beta = 0^\circ$  to  $15^\circ$  was also mapped out. Figure 25b shows the pressure distribution on the vehicle at one of the flow conditions. Figure 26 shows the variation of coefficients of lift and drag and normal forces. The results of these simulations together with the characteristics of the flapping fin described in the previous section were incorporated into the controller development.

Figure 27 shows the force generated by the flapping fins on the hovering NRL-UUV. The surface pressure distribution on the vehicle at one instant during the flapping cycle is shown in Fig. 28. The drag force on the vehicle traveling at  $1\text{kt}$  is  $0.25\text{ N}$ . It is clear that the mean thrust force is sufficient to propel the vehicle to more than  $1\text{ kt}$ . However, the mean negative lift suggests that we need a vehicle controller that is capable of maintaining vertical position while still enabling this forward speed. Hence, the computed results from the parametric studies on the control variables was used in conjunction with the controller design and was successfully tested by J. Geder et al.<sup>22</sup>, using three different control methods, both for vertical level flight and yaw motion.

## **IV. Summary and Conclusions**

Three-dimensional unsteady computations of an actively controlled curvature, flapping fin have been carried out. The computed results are validated against experimental data and the comparison is good. Simulations were performed for flow past a fin test vehicle incorporating



the flapping deforming fins. Several parameters controlling the kinematics of the fin were varied. The fin flapping at 2Hz was able to provide mean positive thrust for a vehicle speed up to 2 kts. To achieve a controlled steady level flight, it is necessary to have kinematics that would yield positive lift forces. Increasing the rigidity of the fin was found to result in mean positive lift, while the thrust generated decreased. Altering the mean stroke bias angle produced a similar effect. These two parameters have been computationally shown to provide a viable set of control parameters for steady level flight and yaw motion of the UUV. The hydrodynamic characteristics of a newly built prototype vehicle at NRL were computed for a range of operational conditions. The propulsion performance of the deforming fins has been computationally demonstrated to provide adequate force production and controllability for the fin test vehicle.

### **Acknowledgments**

This work was supported by ONR through an NRL 6.2 project: “Unsteady Hydrodynamics of Swimming Vehicles.” This work was supported in part by a grant of HPC time from the DoD HPC Center at NRL. The authors would like to thank Prof. Rainald Löhner of George Mason University for his assistance throughout the course of this work.

## References

- [1] Blake R.W., “The mechanics of labriform motion I. Labriform locomotion in the angelfish (*pterophyllum eimekei*): An analysis of the power stroke”, *J. Exp. Biol.*, **82**, 1979, pp. 255-271.
- [2] Platzer, M.F. and Jones, K.D., “Flapping Wing Aerodynamics – Progress and Challenges,” *AIAA 2006-500*, Washington, D.C., January 2006.
- [3] Rozhdestvensky, K.V. and Ryzhov, V.A., “Aerohydrodynamics of Flapping Wing Propulsors,” *Prog. in Aero. Sci.*, Vol. 39, No. 8, 2003, pp. 585-633.
- [4] Shyy, W., Berg, M. and Ljungqvist, D., “Flapping and Flexible Wings for Biological and Micro Air Vehicles,” *Prog. in Aero. Sci.*, Vol. 35, 1999, pp. 455-505.
- [5] Kato, N., Liu, H. and Morikawa, H., “Biology-Inspired Precision Maneuvering of Underwater Vehicles,” *Proc. of the 12<sup>th</sup> Intl. offshore and Polar Engg. Conf.*, Vol. 2, 2002, pp. 269-276.
- [6] Ando, Y., Kato, N., Suzuki, H., Ariyoshi, T., Suzumori, K., Kanda, T. and Endo, S., “Elastic Pectoral Fin Actuators for Biomimetic Underwater Vehicles,” *Proc. of the 16<sup>th</sup> Intl. offshore and Polar Engg. Conf.*, 2006, pp. 260-267.

- [7] Tangorra, J.L., Davidson, S. N., Hunter, I., Madden, P.G.A., Lauder, G.V., Dong, H., Bozukurtas, M. and Mittal, R., “The Development of a Biologically Inspired Propulsor for Unmanned Underwater Vehicles,” *IEEE J. of Ocean Engg.*, Vol. 32, No. 3, July 2007, pp. 533-550.
  
- [8] Walker, J. A. and Westneat, M. W., “Labriform Propulsion in Fishes: Kinematics of Flapping Aquatic Flight in the Bird Wrasse, *Gomphosus Varius*. (Labridae),” *J. Exp. Biol.* **200**, 1997, pp. 1549-1569.
  
- [9] Ramamurti, R., Sandberg, W.C., Löhner, R., Walker, J. A. and Westneat, M. W., “Fluid Dynamics of Flapping Aquatic Flight in the Bird Wrasse: 3-D Unsteady Computations with Fin Deformation,” *J. Exp. Biol.* **205**, 19, October 2002, pp. 2997-3008.
  
- [10] Palmisano, J., Geder, J., Ramamurti, R., Liu, K-J., Cohen, J., Mengesha, T., Naciri, J. Sandberg, W.C. and Ratna, B., “Design, Development and testing of Flapping Fins with Actively Controlled Curvature for an Unmanned Underwater Vehicle,” *Bio-Mechanisms of Swimming and Flying*, Eds. N. Kato and S. Kamimura, Springer, 2007, pp. 283-294.
  
- [11] Ramamurti, R. and Löhner, R., “Evaluation of an Incompressible Flow Solver Based on Simple Elements,” *Advances in Finite Element Analysis in Fluid Dynamics*, FED **137**, Editors: Dhaubhadel, M. N. *et al.*, ASME Publication, New York, 1992, pp. 33-42.

- [12] Ramamurti, R., Löhner, R., and Sandberg, W. C., “Computation of the 3-D Unsteady Flow Past Deforming Geometries,” *Int. J. Comp. Fluid Dyn.*, 13, 1999, pp. 83-99.
- [13] Ramamurti, R. and Sandberg, W.C., “Computational Fluid Dynamics Study for Optimization of a Fin Design,” *Proc. Of the 24<sup>th</sup> AIAA Applied Aerodynamics Conf.*, AIAA-2006-3658, San Francisco, CA, 2006.
- [14] Ramamurti, R., Sandberg, W.C. and Löhner, R., “The Influence of Fin Rigidity and Gusts on the Force Production in Fishes and Insects: A Computational Study,” *AIAA-2004-0404*, Washington, DC, January 2004.
- [15] Trease, B.P., Lu, K.J. and Kota, S., “Biomimetic Compliant System for Smart Actuator-Driven Aquatic Propulsion: Preliminary Results,” *ASME International Mechanical Engineering Congress & Exposition*, Washington, D.C., IMEC2003-41446, 2003.
- [16] Palmisano, J., Geder, J., Ramamurti, R., Sandberg, W.C. and Ratna, B., “Real-Time Robotic Pectoral Fin CPG Using Weighted Gait Combinations,” in review, submitted to *IEEE Transactions on Robotics*, September 2008.
- [17] Geder, J., Sandberg, W.C. and Ramamurti, R., “Multi-Camera, High-Speed Imaging System for Kinematics Data Collection,” *NRL Memorandum report NRL/MR/6401--07-9054*, September 2007.

- [18] Bohl, D.G. and Koochesfahani, M.M., “MTV Measurements of the Vortical Field in the Wake of an Airfoil Oscillating at High Reduced Frequency,” *J. Fluid Mech.*, Vol. 620, 2009, pp. 63-88.
- [19] Ramamurti, R. and Sandberg, W.C., “ Simulation of Flow about Flapping Airfoils Using Finite Element Incompressible Flow Solver,” *AIAA J.*, Vol. 39, No. 2, 2001, pp. 253-260.
- [20] Smagorinsky, J., “General Circulation Experiments with the Primitive Equations. I. The Basic Experiment,” *Month. Wea. Rev.*, 91, 1963, pp. 99-164.
- [21] Ramamurti, R. and Sandberg, W.C., “A Three-Dimensional Computational Study of the Aerodynamic Mechanisms of Insect Flight,” *J. Exp. Biol.*, 205, 2002, 1507-1518.
- [22] Geder, J., Palmisano, J., Ramamurti, R., Sandberg, W.C. and Ratna, B., “Fuzzy Logic PID Based Control Design and Performance for a Pectoral Fin Propelled Unmanned Underwater Vehicle,” *Proc. of the Intl. Conf. on Control, Automation and Systems*, Seoul, South Korea, October 2008.

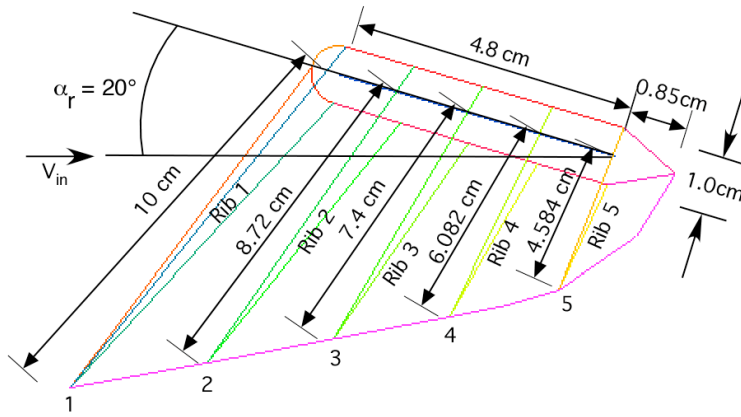


Fig. 1. Schematic of the deforming fin showing the root cross-section and the 5 ribs.

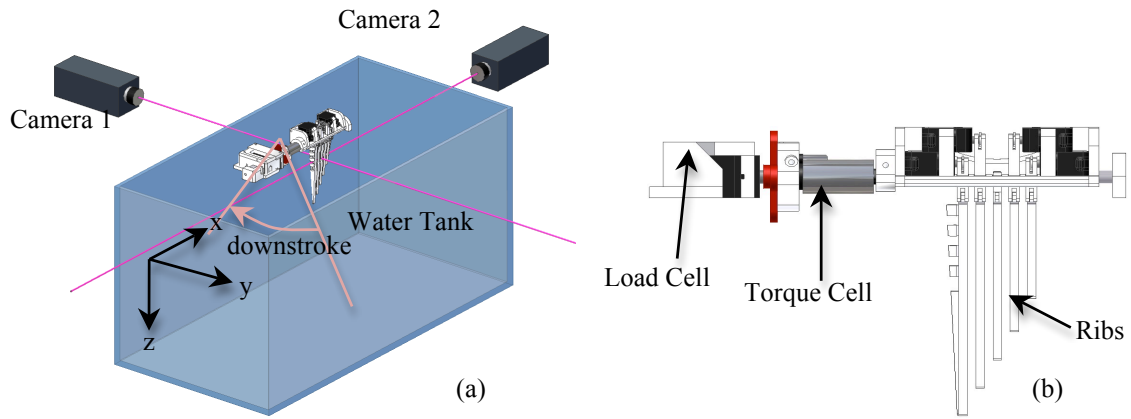


Fig. 2. Experimental setup, (a) tank and camera locations and (b) side view of the fin and sensor locations.

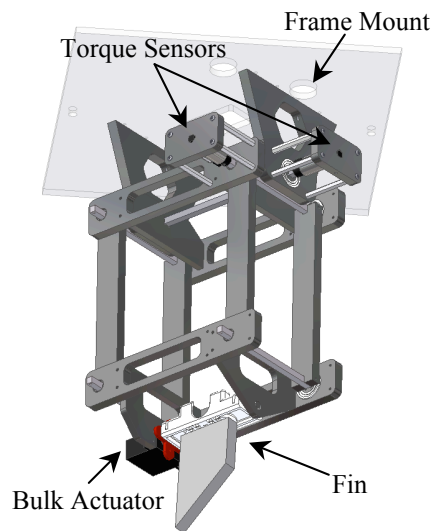


Fig. 3. Modified fin forces measuring device.

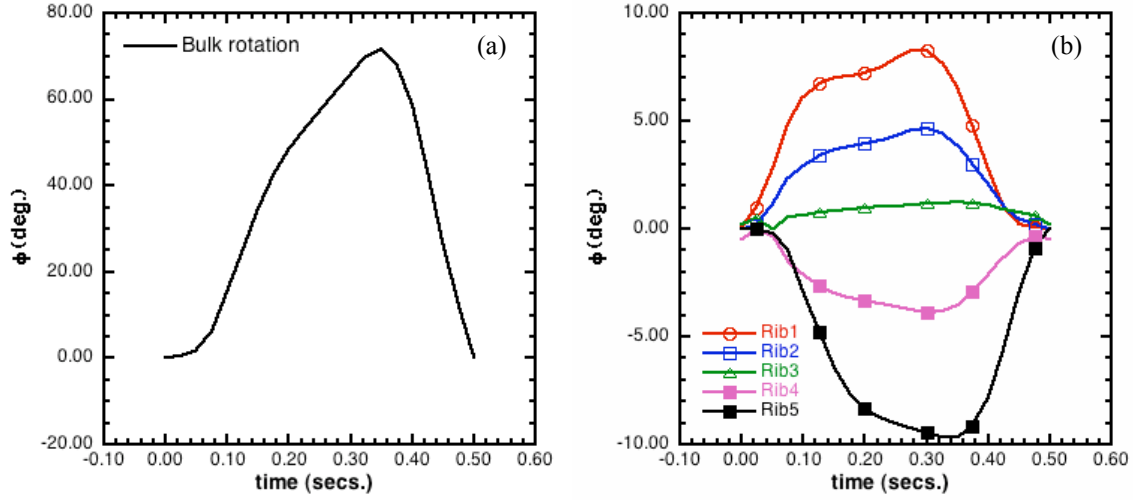


Fig. 4. Baseline Kinematics,  $f = 2.0$  Hz, (a) Bulk rotation and (b) relative rib rotation.

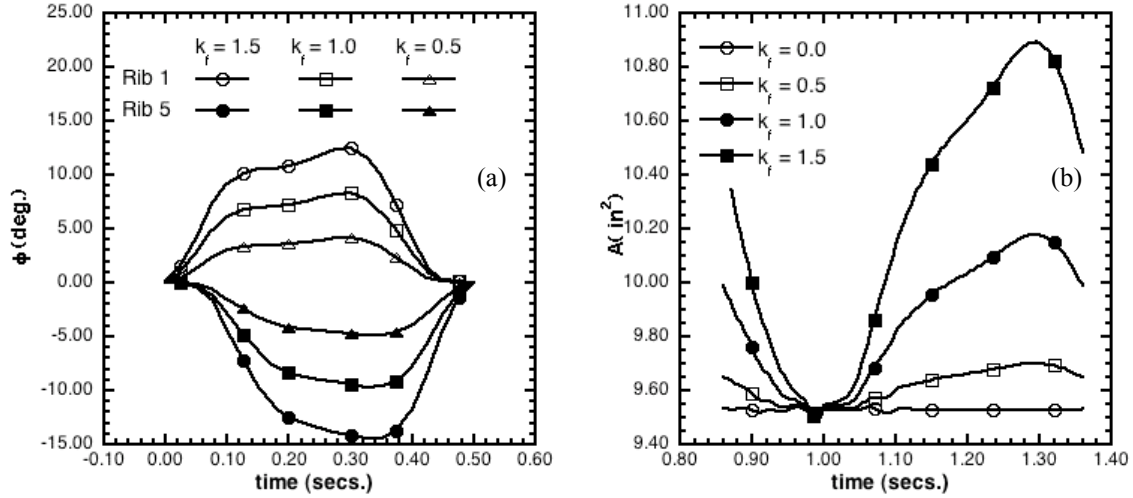


Fig. 5. Effect of controlled deformation on (a) the relative rotation of leading and trailing edge ribs and (b) the wetted surface area of the fin.

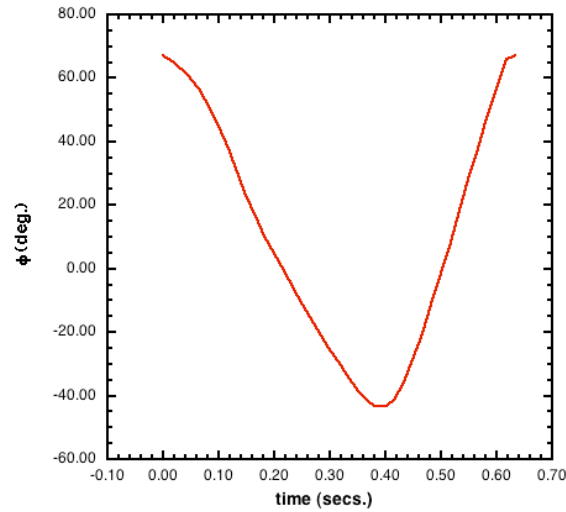


Fig. 6. Kinematics for a rigid fin flapping at 1.579 Hz.

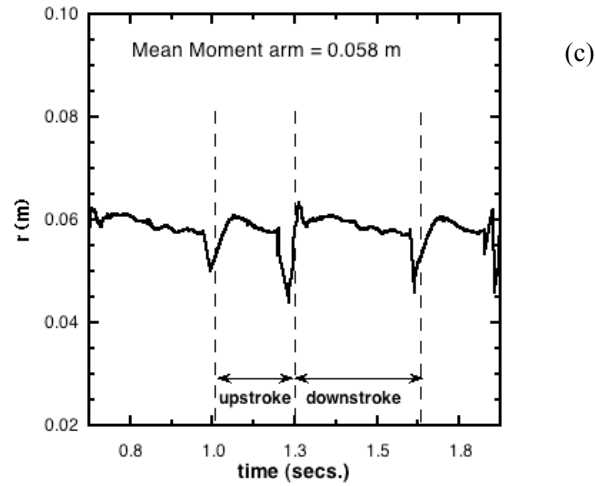
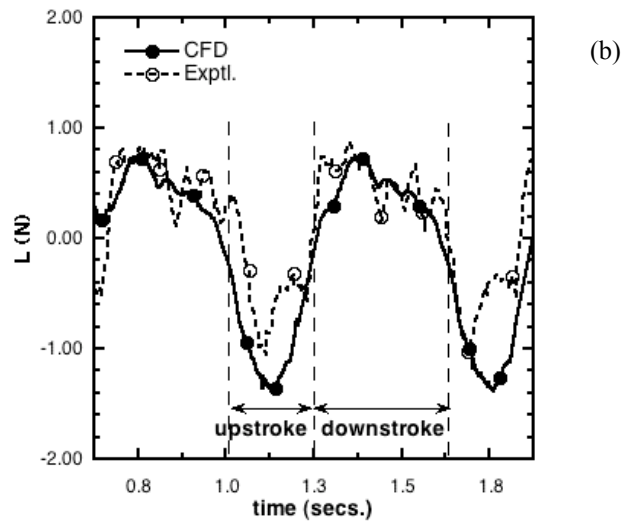
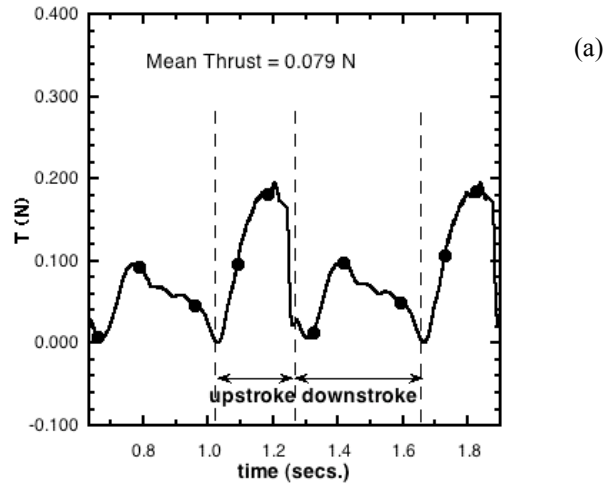


Fig. 7. Variation of (a) thrust , (b) lift and (c) mean center of pressure from a fin flapping at 1.579Hz,  $V = 0$ kts.



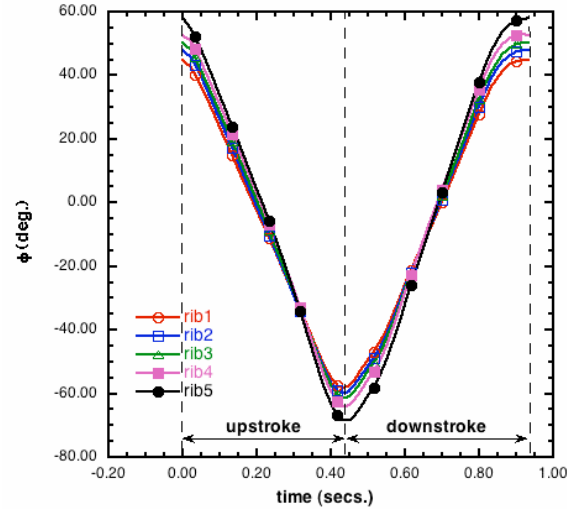


Fig. 8. Kinematics of a deforming fin,  $f = 1.0715\text{Hz}$ ,  $V = 0\text{kts}$ .

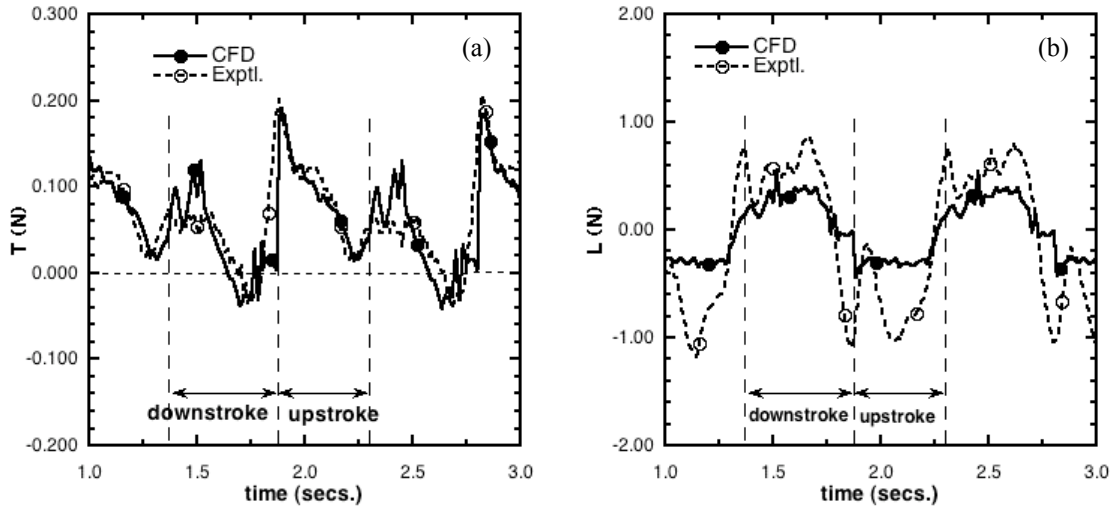


Fig. 9. Comparison of Force production for a deforming fin,  $f = 1.0715\text{Hz}$ ,  $V = 0\text{kts}$ .

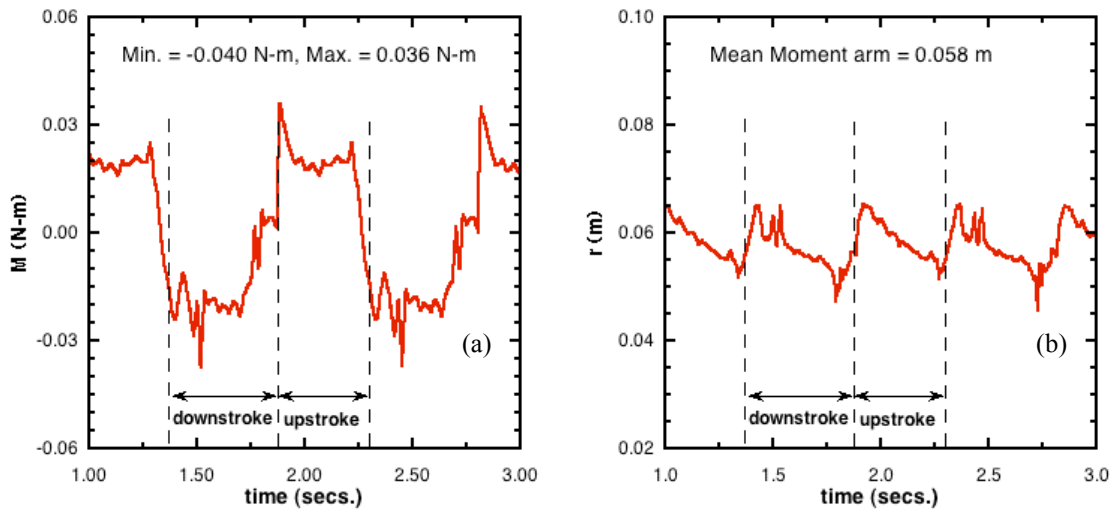


Fig. 10. Results from a flapping deforming fin,  $f = 1.0715\text{ Hz}$ ,  $V = 0\text{kts}$ , (a) moment about axis of rotation and (b) center of pressure.

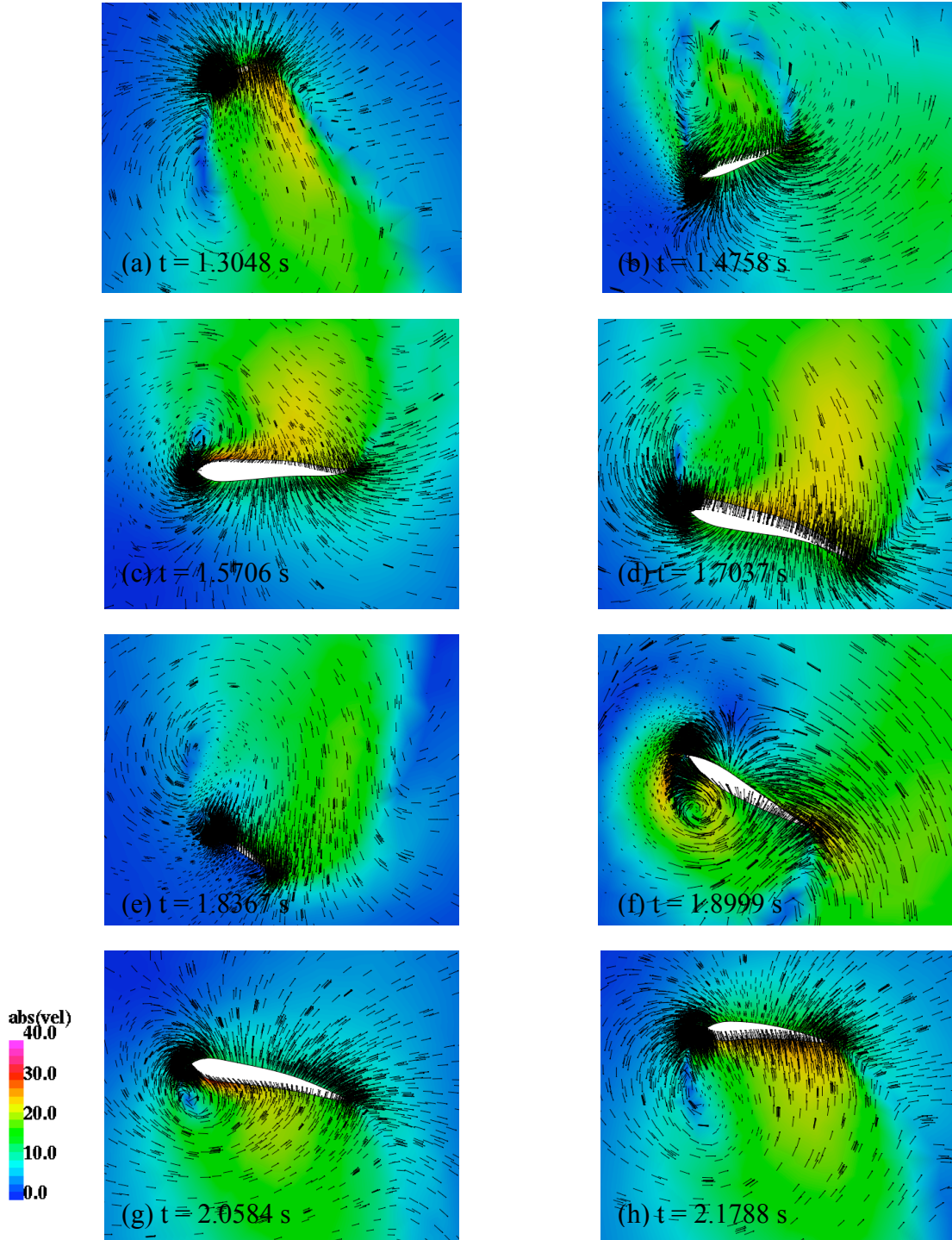


Fig. 11. Velocity vectors on a plane cut at  $x = 0.0508\text{m}$  from the root of the fin, showing the evolution of the leading and trailing edge vortices during the downstroke (a-e) and the upstroke (f-h).

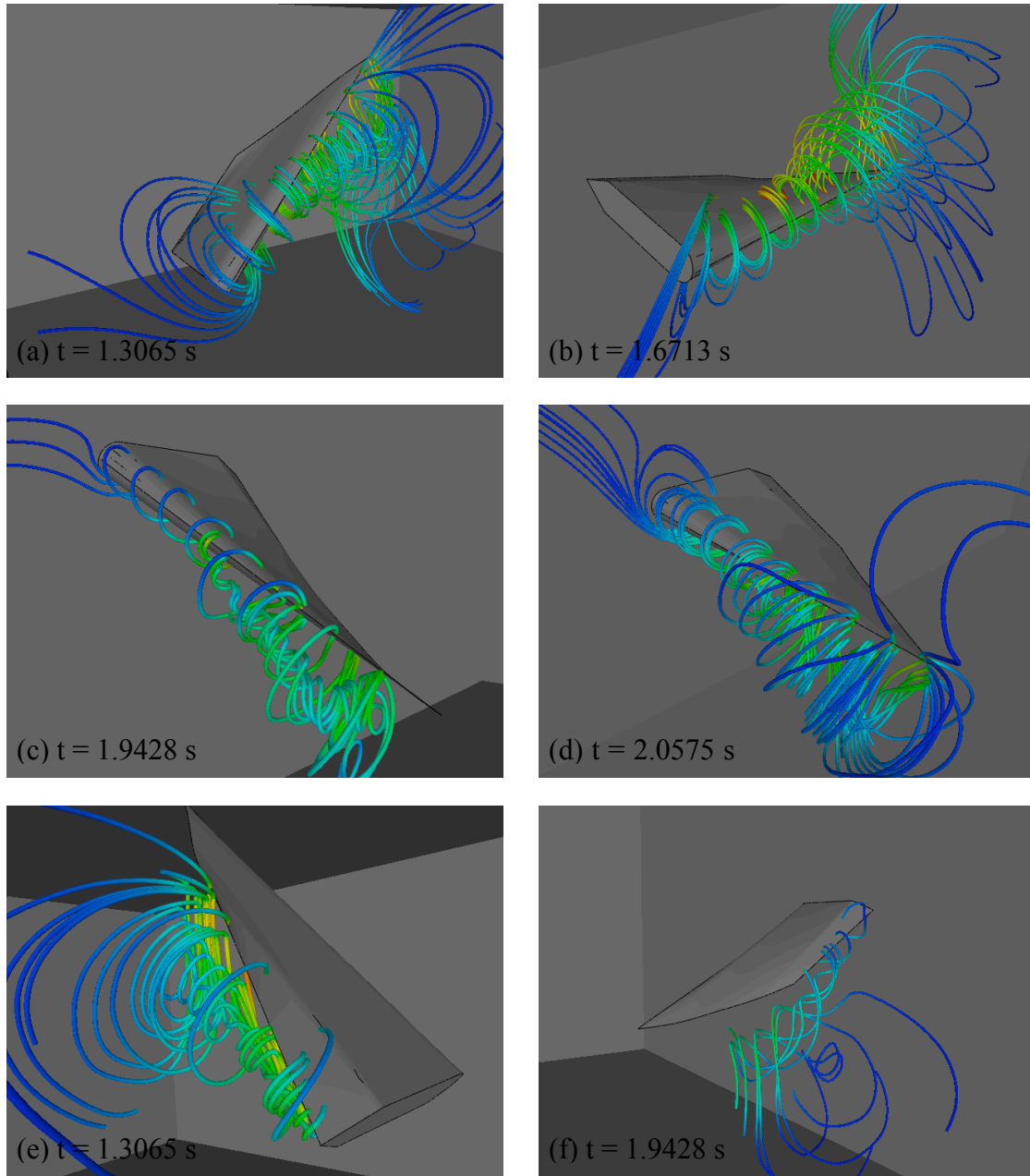


Fig. 12. Instantaneous particle traces released from a rake in front of the leading edge (a-d) and after the trailing edge (f and g).

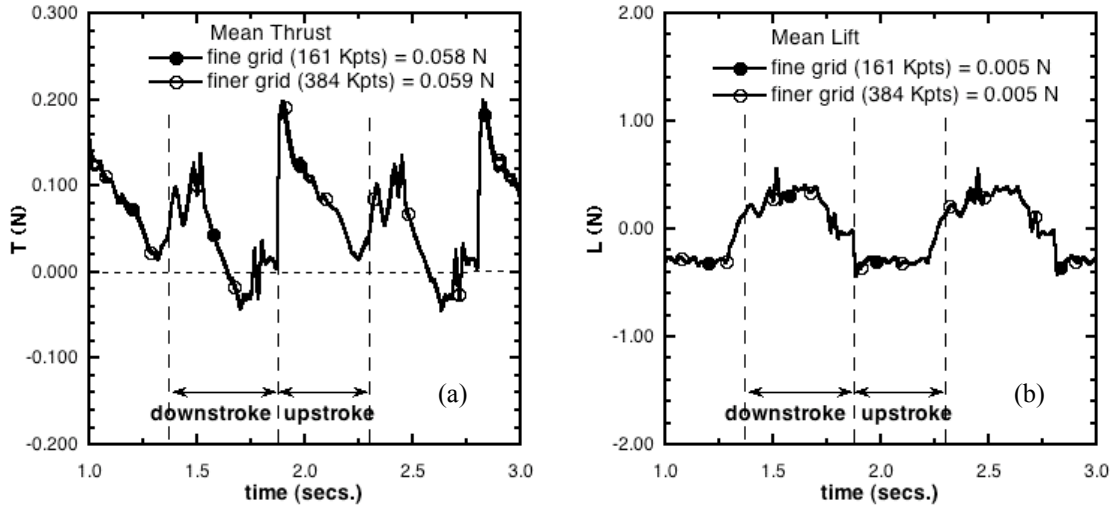


Fig. 13. Effect of grid refinement on the force production.

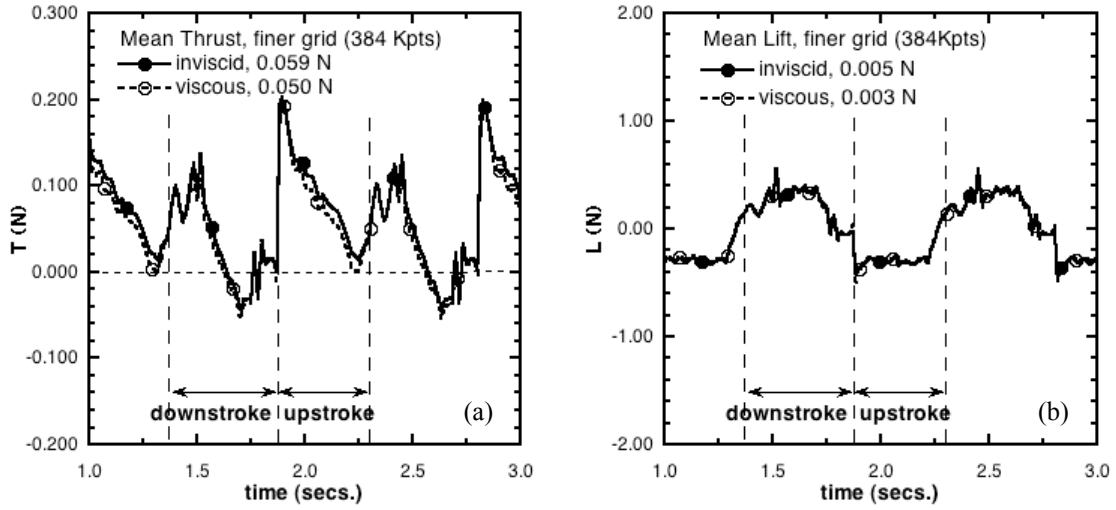


Fig. 14. Effect of viscosity on the force production.

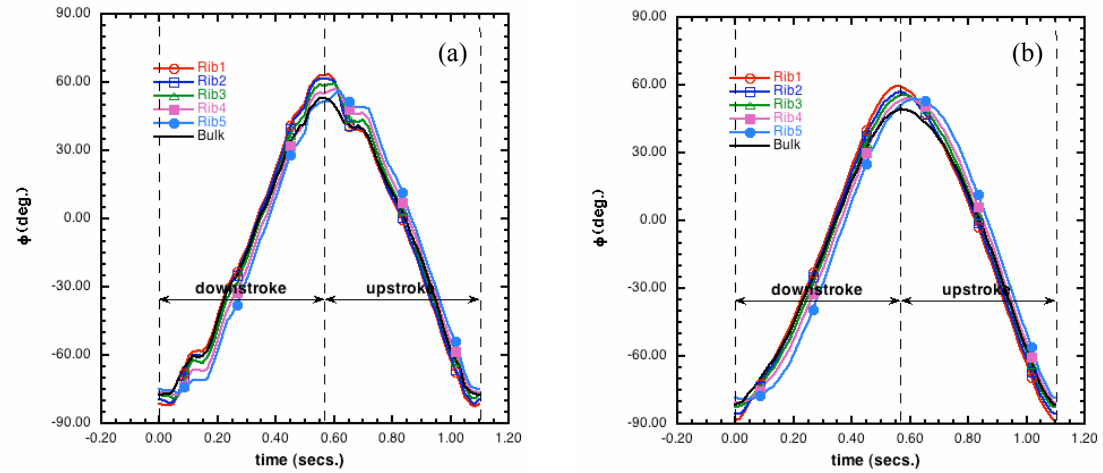


Fig. 15. Kinematics for a flapping deforming fin,  $f = 0.9091$  Hz, from (a) raw data and (b) smoothed data.

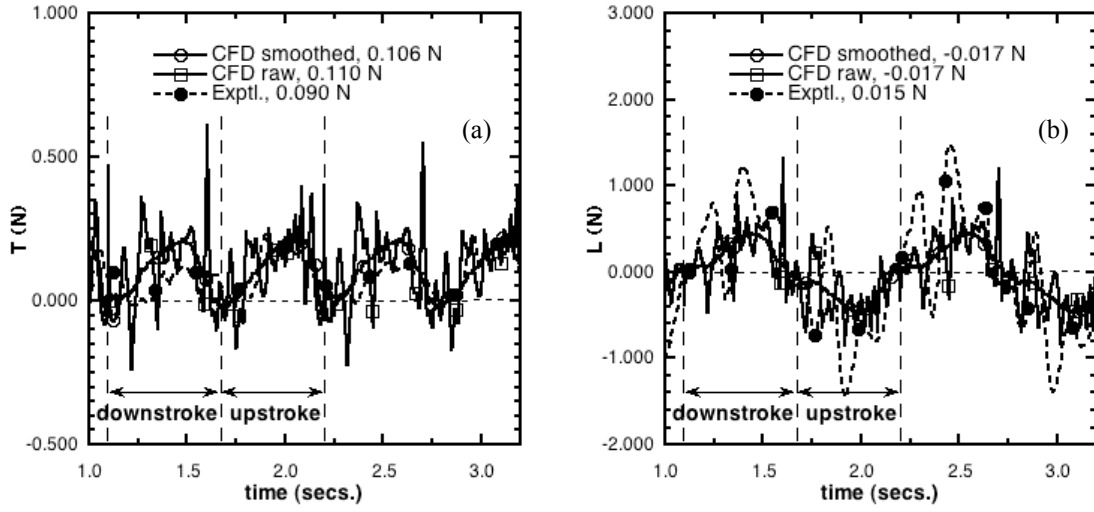


Fig. 16. Comparison of Force production for a deforming fin,  $f = 0.9091\text{Hz}$ ,  $V = 0\text{kts}$ .

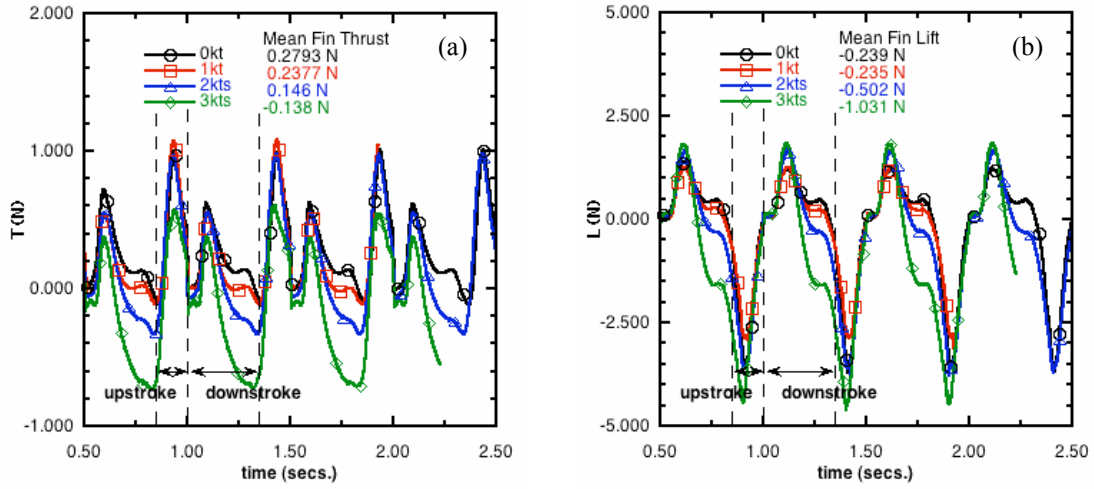


Fig. 17. Effect of vehicle speed on the thrust and lift production,  $f = 2.0\text{Hz}$ ,  $k_f = 1.5$ .

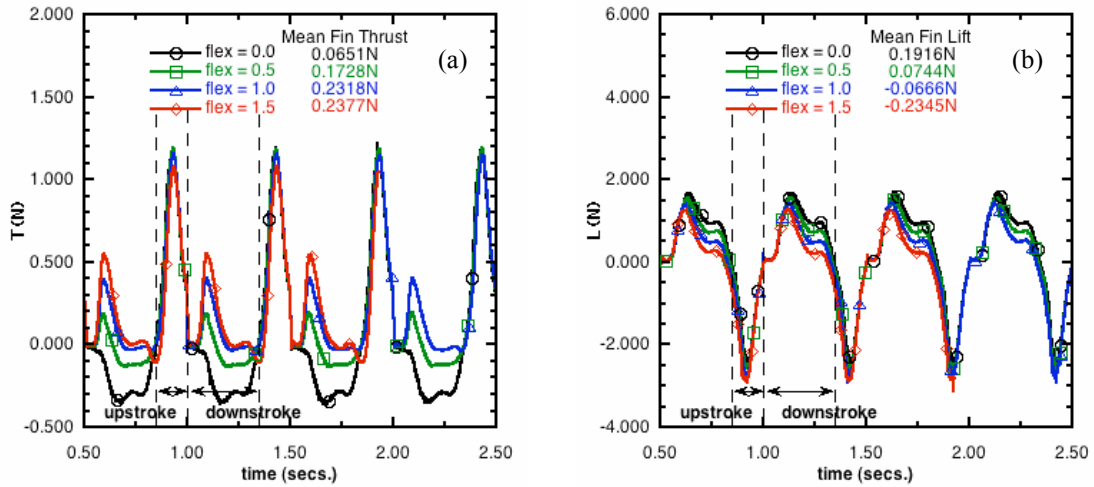


Fig. 18. Effect of flexibility on the thrust and lift production,  $f = 2.0\text{Hz}$ ,  $V = 1\text{kt}$ .

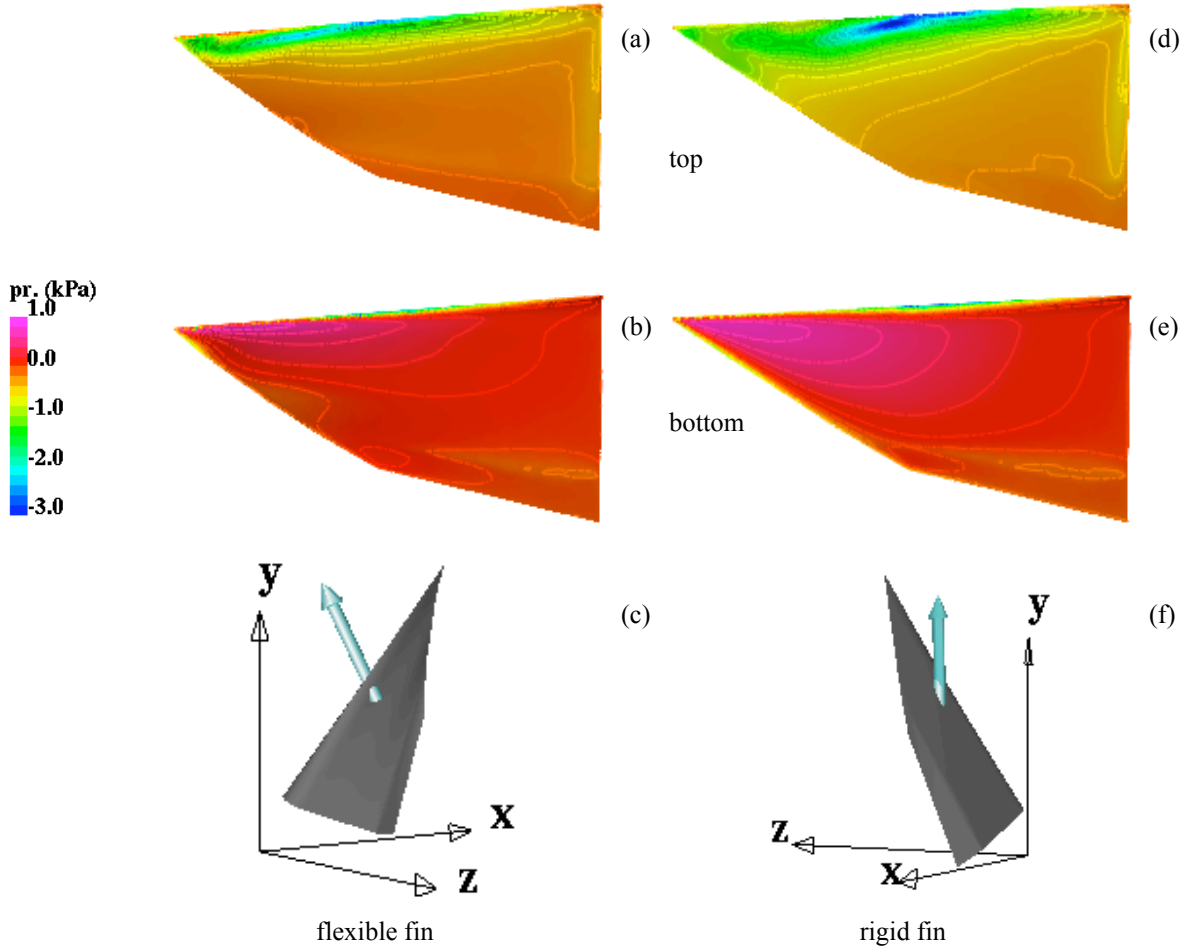


Fig. 19. Comparison of surface pressure distribution and force vector during downstroke,  $t = 1.09s$ ,  $f = 2.0Hz$ ,  $V = 1.0$  kt. (a-c) flexible fin, (d-f) rigid fin.

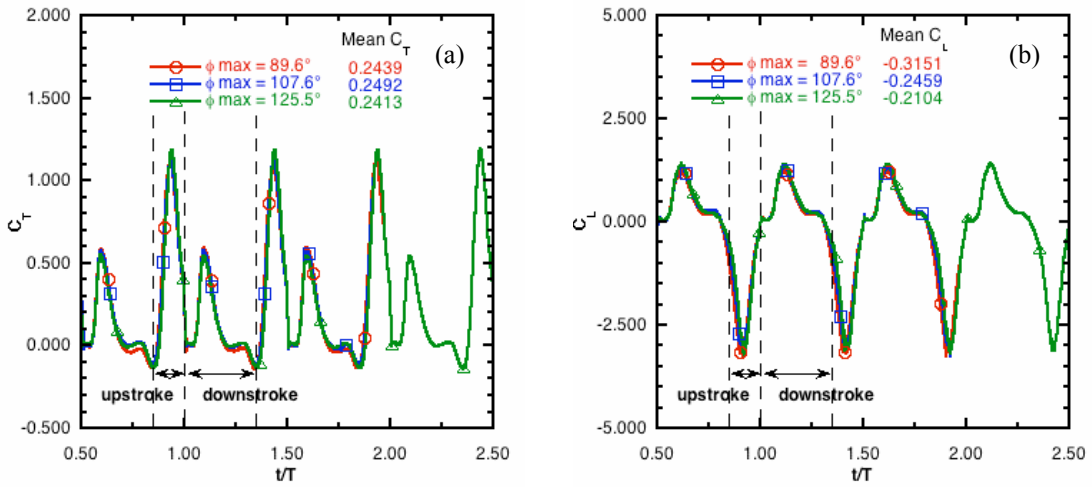


Fig. 20. Time history of coefficients of thrust and lift for various bulk amplitudes,  $f = 2.0$  Hz,  $V = 1$  kt.



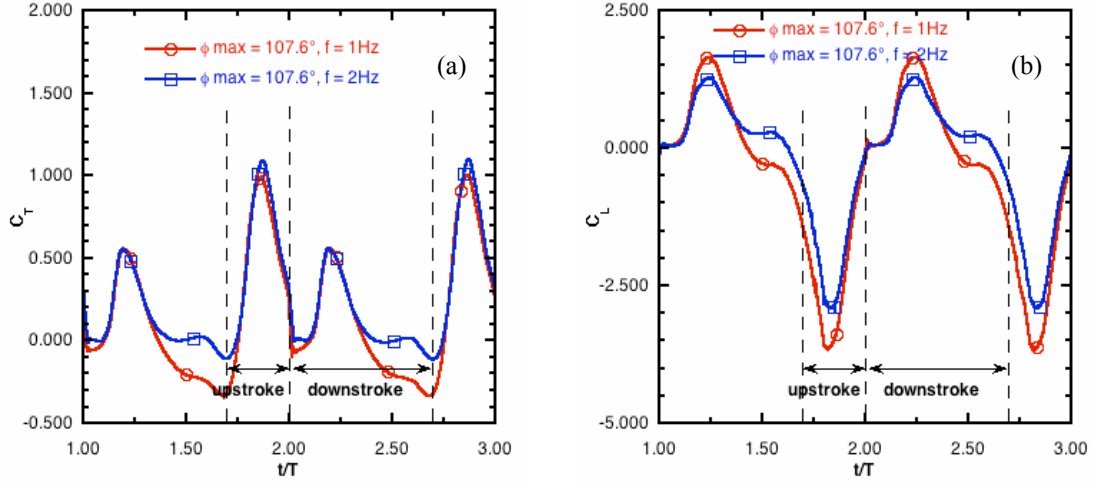


Fig. 21. Effect of flapping frequency on the thrust and lift coefficients,  $V = 1$  kt.

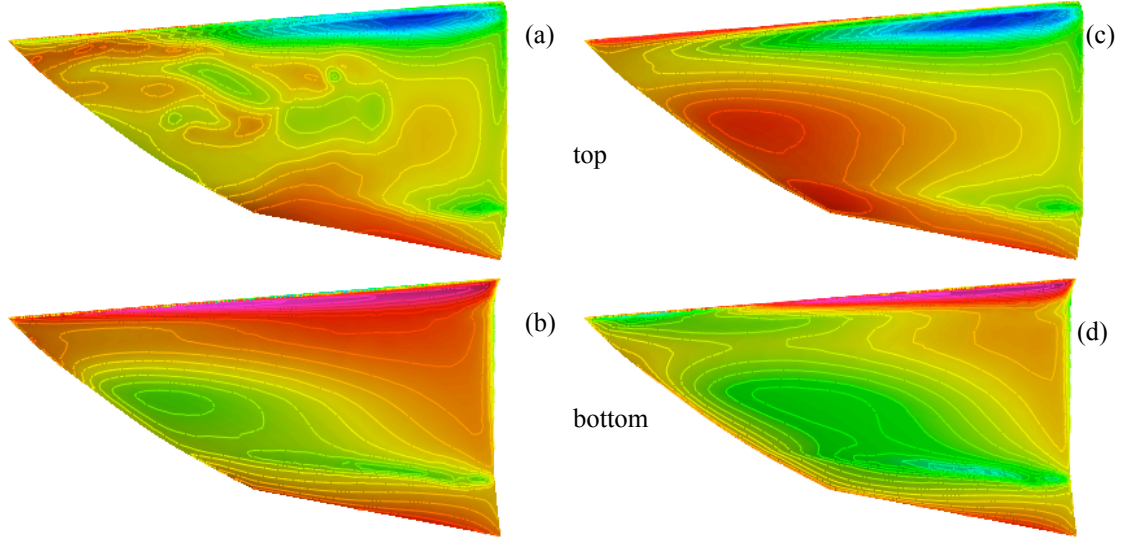


Fig. 22. Surface Pressure distribution on the fin at  $t/T = 2.5$ , (a,b)  $f = 1$  Hz and (c,d)  $f = 2$  Hz.

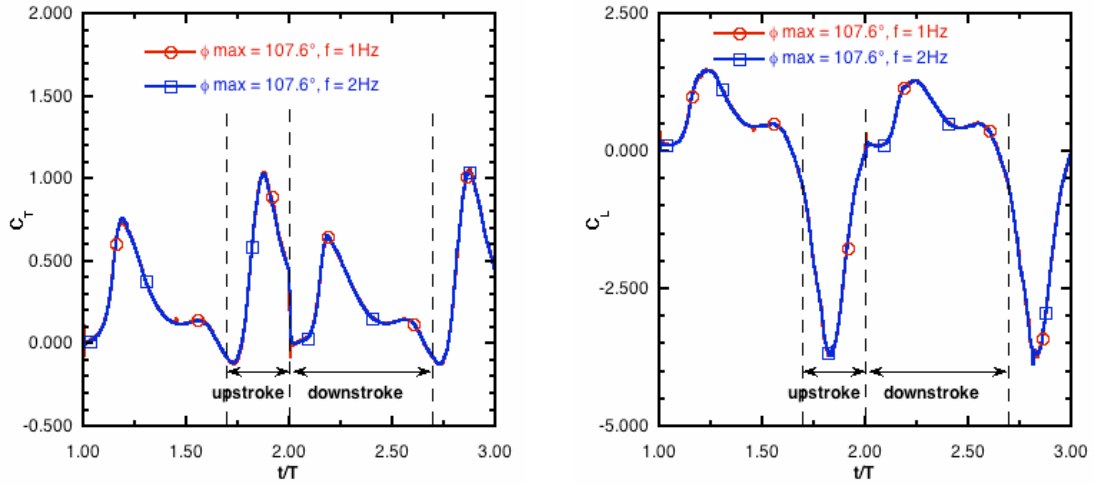


Fig. 23. Effect of flapping frequency on the thrust and lift coefficients,  $V = 0$  kt.

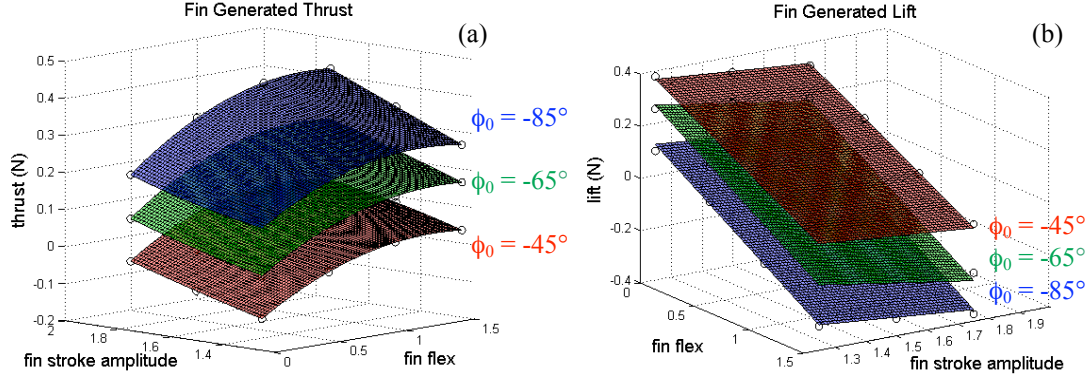


Fig. 24. Mean thrust and lift forces generated by the flapping fin,  $f = 2.0$  Hz,  $V = 1.0$  kt.

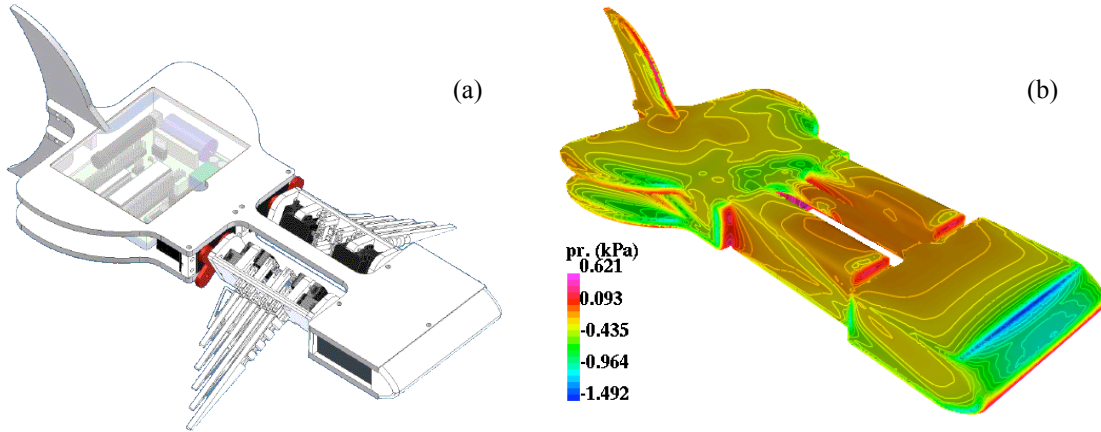


Fig. 25. (a) NRL-UUV test vehicle for carrying a set of two actively controlled curvature fins and (b) Surface pressure distribution on NRL-UUV swimming at 2kts,  $\alpha = 20^\circ$ ,  $\beta = 0^\circ$ .

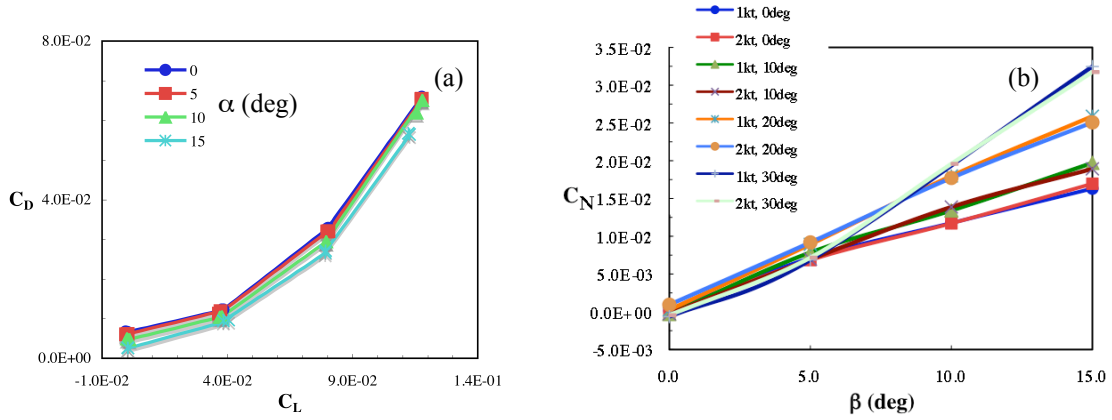


Fig. 26. Hydrodynamics characteristics of the NRL-UUV.



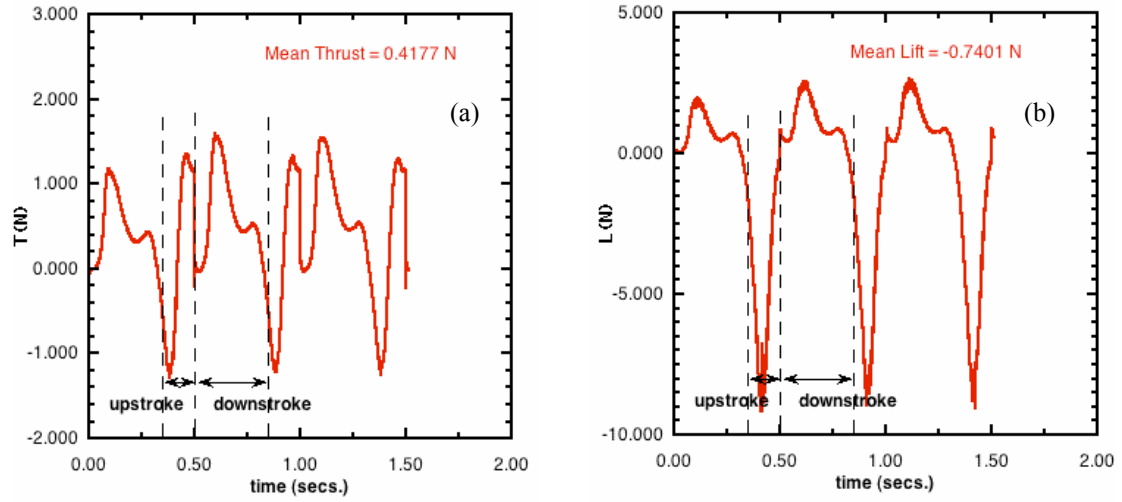


Fig. 27. Thrust and lift production on a hovering NRL-UUV with fins flapping at 2 Hz.

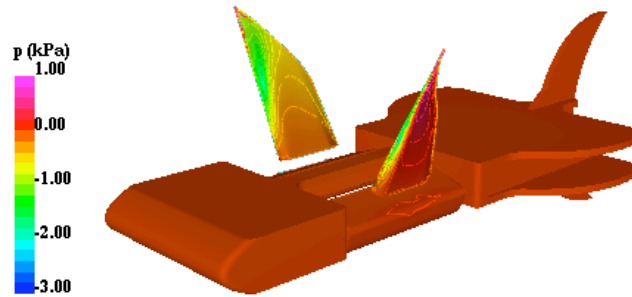


Fig. 28. Surface pressure distribution on a hovering NRL-UUV at  $t = 1.09$  s.